Fatigue Analysis of Unanchored Steel Liquid Storage Tank Shell-to-Base Connections during Earthquake Induced Uplift

G.S. Prinz, A. Nussbaumer
Steel Structures Laboratory (ICOM), Ecole Polytechnique Federale de Lausanne (EPFL), Lausanne, Switzerland

G. Cortes
*LeTourneau University, Longview, Texas, USA*

SUMMARY:
During severe seismic events the base of unanchored steel liquid-storage tanks can uplift causing large inelastic rotation demands and possible low-cycle fatigue failure at the shell-to-base connections. Current code provisions limit uplift rotations to 0.2rad; however, limited research exists on the rotation capacity of shell-to-base connections. Previous studies are limited to constant amplitude static demands, and neglect the presence of multi-axial stress states which have the potential to reduce capacity. In this paper, the performance of tank shell-to-base connections are analyzed under uplift histories generated from realistic earthquake ground motions. Uplift histories from design-level earthquake motions are applied to two axi-symmetric finite element models representing two tank geometries (broad and slender tanks), and fatigue damage is assessed using a calibrated stress modified critical strain low-cycle fatigue criterion. Results from analyses indicate excess capacity in the shell-to-base connection whereas the EC8 provisions indicate failure (exceedance of 0.2rad).

Key Words: Unanchored steel tanks; low cycle fatigue; finite element analysis.

1. INTRODUCTION

Unanchored steel liquid storage tanks can rock during extreme seismic events, damaging the welded connection between the tank shell and the tank base. Rocking and uplift of the tank base can create large inelastic rotation demands at the welded shell-to-base connections and large multi-axial membrane loads in the tank base-plate due to cylindrical geometric effects (see Figure 1) (Fujikazu et al., 1988; Peek, 1988; Peek and Jennings, 1988; Koller and Malhotra, 2004). Repeated cycles of uplift can lead to low-cycle fatigue fractures and ultimately spillage of tank contents.
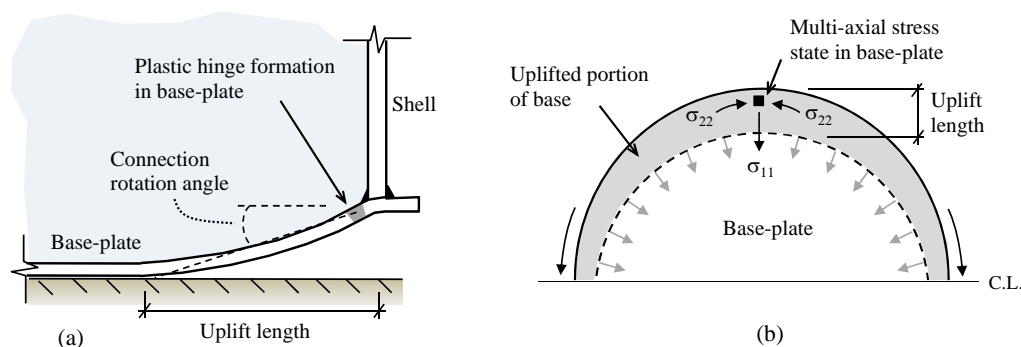
Figure 1. (a) Plastic hinge in tank base during uplift; and (b) multi-axial stress state during uplift (Prinz and Nussbaumer, 2012b)

Current tank design standards limit the rotation capacity of the shell-to-base connections to less than 0.2rad, for an unspecified number of uplift cycles (Eurocode 8, 1998; NZSEE, 2009). This rotation limit is based on an assumed allowable base-plate strain of 5%. There is no clear background to justify this 5% strain limit, and recent fatigue testing indicates that the limit may be overly conservative (Cortes et al., 2011; Prinz and Nussbaumer, 2012a).

Experimental testing by Cortes et al. (2011) and Prinz and Nussbaumer (2012a) demonstrate that tank connection fatigue capacity is governed by the ductility of the base-plate base material, as fractures originate away from the weld toe and weld heat affected zone. In Prinz and Nussbaumer (2012a), 27 connections fabricated from S235 and S355 steel (having typical fracture strains near 0.38% and between 0.19 and 0.36% respectively) were tested to failure under constant range cycles with an applied radial-membrane load equal to 10% of the nominal yield load ($10\%\sigma_y$). Tank connections fabricated of S235 steel achieved 161 cycles, on average, at 0.4rad prior to complete rupture of the connection. One S235 specimen achieved 177 cycles at 0.4rad prior to complete rupture, with initial penetration of the fatigue crack through the base-plate (initial leakage condition) occurring after 166 cycles. Multi-axial stress states were not considered in either experimental study, as circumferential compression was not included in the tested connections. Variable range loading effects were also not fully considered as specimens were subjected to constant range cycles.

A recent analytical study suggests that multi-axial stress states can significantly reduce fatigue capacity (Prinz and Nussbaumer, 2012b). In Prinz and Nussbaumer (2012b), 24 shell-to-base connections were analyzed under various ranges of rotation with various amounts of circumferential compression and radial tension. Analyses indicated that moderate levels of circumferential compression, when combined with radial tension, can reduce fatigue capacity up to 45%. Smaller uplift cycles contributed more to damage than previously assumed using linear damage models.

In this study, shell-to-base connection models representing three tanks from within Switzerland are subjected to realistic variable-range uplift histories, with realistic multi-axial applied stresses, generated from realistic dynamic earthquake motions. Uplift histories determined from dynamically loaded global tank models are applied to detailed connection sub-models. Axi-symmetric element formulations are used to capture the varying multi-axial conditions during uplift. The paper begins by describing the modeling techniques used, including model geometry, materials, elements, and applied uplift histories. Next, a stress modified critical strain damage model is presented along with discussion of calibration procedures. Following, analytical results are presented and lastly conclusions regarding the performance of tank connections under realistic uplift loading are provided.

2. FATIGUE SIMULATIONS

2.1. Model Geometry and Material Behavior

Two existing tanks from different cities in Switzerland (Rumlang and Mellingen) were chosen for the fatigue study. The two tanks represent both broad and slender tank geometries, having different height-to-radius ratios (H/R ratios). The Rumlang tank, with an H/R ratio greater than 1.5, represents a slender geometry; while the Mellingen tank, with an H/R ratio of 1.14, represents a broad geometry.

Typically, tanks are constructed with a thin steel base welded to a thicker reinforcing ring at the base edge, which is then attached to the often thicker shell. This thicker reinforcing ring supports the additional weight of the tank shell. Figure 2 shows a typical tank connection detail, using the Rumlang dimensions as an example. Table 1 presents the dimensions for each tank, including height, radius, connection plate thicknesses, and natural frequency (determined using EC8 procedures). Note in Table 1 that the base-plate thickness represents the thickness of the reinforcing ring which is welded to the tank shell (the base thickness at the shell-to-base connection). Weld geometry was considered in all connection models with a fillet radius of 1mm used between the weld toe and base reinforcing ring to avoid abrupt geometric changes. ABAQUS was used for the two analyses.

Table 1: Tank Geometry

Tank ID	Height [m]	Radius [m]	Impulsive Mass Height [m]	Base-Plate Thickness [mm]	Shell Thickness [mm]	Natural Frequency [Hz]
Rumlang	26	15	12	12	15.5	2.8
Mellingen	25	22	10.5	18	27	3.6
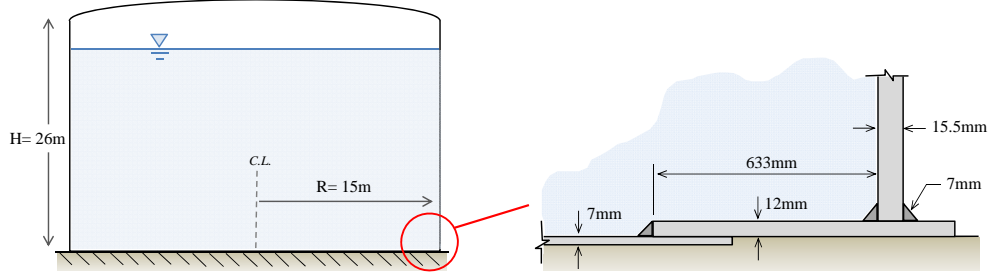
Figure 2. Tank geometry and shell-to-base connection detail for Rumlang tank.

Tensile coupon testing of S355 steel was used to calibrate the material parameters for each model. The S355 tensile coupons were tested using a 200kN universal testing machine in accordance with ASTM Standard *E8* (ASTM, 2002). A linear kinematic hardening model was used to simulate the material behavior. Because fractures in the experimental testing of tank connections originated in the base material above the weld toe (Prinz and Nussbaumer, 2012a), the same material properties were assigned to the shell, base-plate, and welds. Large displacement effects were accounted for using the nonlinear geometry option in ABAQUS.

2.2. Element Formulation and Boundary Conditions

Due to the cylindrical geometry of the steel tank, 2-D axisymmetric finite elements are used to simulate the welded shell-to-base connection. Four-node linear axisymmetric solid elements with reduced integration (CAX4R in ABAQUS) model the base-plate/reinforcing ring, shell, and fillet welds. Using 2-D axisymmetric elements reduces computational effort while providing realistic multi-axial strain states from out-of-plane confinement and geometric effects.

Axisymmetric boundary conditions and vertical rollers simulate the surrounding tank structure. The tank foundation is simulated with multiple compression-only springs. Rollers located above the shell-to-base connection keep the tank shell vertical during uplift and during the applied hydrostatic pressure. The hydrostatic pressure chosen in this study corresponds to a fluid (ρ =800 kg/m^3) height equal to 85% of the total tank height. Compression-only springs simulate an essentially rigid foundation while providing almost no resistance during uplift. Friction between the ground and foundation is not considered. Figure 3 shows the applied constraints and foundation springs for the tank model.
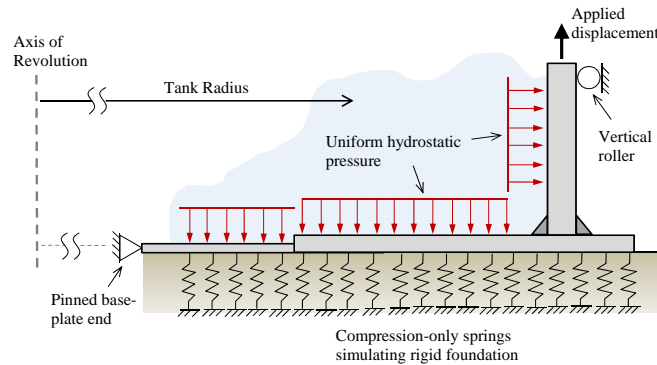

Figure 3. Tank connection boundary conditions and applied loading.

2.3. Mesh Refinement

To provide sufficient strain accuracy for the models in this study, element size near the welded shell-to-base connection was reduced to around 0.2mm. This provided multiple elements throughout the base-plate thickness near the assumed plastic region and sufficiently captured strain gradients near the weld toe for later fatigue evaluation. Outside the weld region, element size was increased to 2mm to reduce computation effort. Figure 4 shows the model mesh with refinement at the connection.
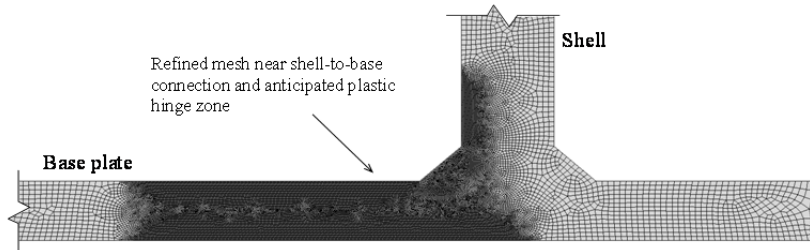
Figure 4. Rumlang tank model mesh with refinement near shell-to-base connection.

3. UPLIFT HISTORIES

Uplift histories resulting from realistic seismic accelerations were used to load each connection model. The uplift histories were generated from a global tank model analyzed in Prinz and Nussbaumer (2012a) using the Open System for Earthquake Engineering Simulation (OpenSEES) (McKenna, 1997). The earthquake ground motion applied to the global tank model was artificially created following procedures outlined in Sabetta and Pugliese (1996), to match the design response spectrum from the seismic prone region of Sion Switzerland (generated using Section 1 of Eurocode 8 (1998) with seismic zone 3b, an assumed soil class C, and 5% viscous damping). An artificial ground motion was used due to the lack of recorded motions within the region. The chosen design spectrum is based on a seismic event with a reference return period of 475 years. Parameters considered for the synthetic ground motion generation include: deep soils, earthquake surface wave magnitude of Ms7.2, and an epicentral distance of 22km. Figure 5(c) shows the design response spectrum for the Sion tank site along with the earthquake response spectrum. Figure 5(a) and (b) presents the applied earthquake acceleration and resulting uplift demands for each tank geometry. Resulting uplift demands were applied to the detailed connection sub-models to assess fatigue damage. To reduce computational effort, uplift demands less than 19mm (0.75in.) were removed from the applied uplift histories. Peak uplift values for each tank are similar to those calculated in other studies (Koller and Malhotra, 2004; Koller, 2003).
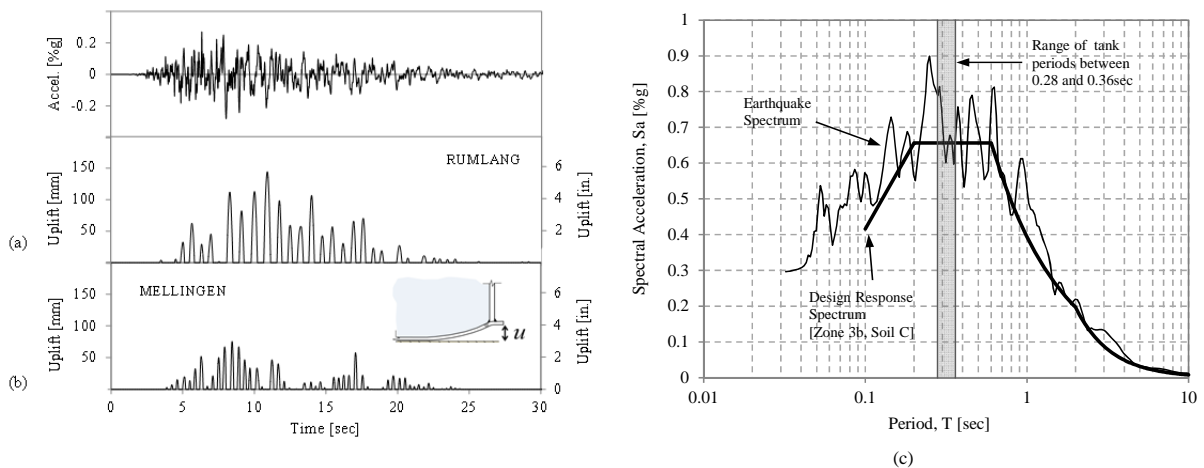
Figure 5. Earthquake acceleration time-histories and corresponding base uplift response for (a) slender Rumlang tank (b) broad Mellingen tank; (c) Earthquake response spectrum and design response spectrum.

4. FATIGUE DAMAGE MODEL

A low-cycle fatigue failure index based on a stress modified critical strain (SMCS) criterion was used to estimate fatigue damage in the two connection models. The failure index is computed as the accumulated equivalent plastic strain, $\bar{\varepsilon}_P$, divided by a critical plastic strain, $\varepsilon_{p,critical}$ presented in Equation 4.1 (Hancock, 1976).

$$\varepsilon_{p,critical} = \alpha \ \exp\left(-\frac{3\sigma_m}{2\sigma_e}\right) \tag{4.1}$$

In Equation 4.1, σ_m is the hydrostatic stress, σ_e is the von Mises stress, and α is a material toughness index. The ratio of the hydrostatic and von Mises stress is the stress triaxiality. Fracture initiation is indicated when the failure index ($\bar{\varepsilon}_P / \varepsilon_{p,critical}$) exceeds 1.0 over a characteristic length, l^*, representative of void coalescence in the material. Calibration of the SMCS parameter l^* is somewhat subjective, requiring interpretation and measurement of microstructural voids on the specimen fracture surface. Because l^* represents a critical volume of coalesced material voids, values are typically small, around 0.1-0.2mm. The calibrated l^* value for A572 Grade 50 steel (similar in strength and ductility to the S355 steel assumed in this study), is 0.198mm (Kanvinde and Deierlein, 2004).

4.1. Calibration of Critical Strain ($\varepsilon_{p,critical}$) Parameter α

In addition to l^*, the material specific parameter α must be calibrated. Historically, calibration of α requires both finite element simulation and experimental coupon testing (Kanvinde and Deierlein, 2006); however, recent research by Myers et al. (2010) demonstrates reasonable determination of α from circumferentially-notched tensile (CNT) testing alone. In Myers et al., empirical expressions were derived for the stress triaxiality and critical strain as functions of the CNT initial and deformed geometries, which can be used to determine α from the relationship in Equation 4.1. The empirical equations for triaxiality and critical strain are (Myers et al., 2010):

$$T' = \left[\frac{1}{3} + \ln\left(\frac{D_{NR}}{4R_N} + 1\right)\right] \cdot \left[1.14 - 0.248 \cdot \ln\left(\frac{D_{NR} \cdot n}{R_N}\right)\right] \tag{4.2}$$

$$\varepsilon'_{p,critical} = 2\ln\left(\frac{D_{NR}}{D_{NR,f}}\right) \cdot \left[0.822 - 0.182 \cdot \ln\left(\frac{D_{NR} \cdot n}{R_N}\right)\right] \tag{4.3}$$

where, T', D_{NR}, $D_{NR,f}$, R_N, n, $\varepsilon'_{p,critical}$ are the derived stress triaxiality, notched root diameter, post-fracture notched root diameter, notch radius, material hardening coefficient, and derived critical strain respectively.

To calibrate α for the materials in this study, four CNT specimens of S355 steel were fabricated from 10mm rolled steel plates and tested to failure in tension according to ASTM Standard *E8* (ASTM, 2002). The three CNT specimens had a 24mm gauge length, 6mm diameter, 3mm notched root diameter, and a notch radius of 1.5mm. Figure 6 shows the CNT specimen geometry. All specimens were tested in a 25 kN capacity universal testing machine and the use of optical extensometers allowed for both transverse and longitudinal strain measurements at the notch.

The material hardening parameter, initial specimen geometry, and deformed geometry results were incorporated into Equations 2 and 3, and α was determined for each specimen. The material hardening parameter, n, was determined from the true-stress true-strain relationship and the power-law equation $\sigma_t = A\varepsilon_t^n$. Table 2 presents a summary of the individual calibration results, including determined values of T', $\varepsilon'_{p,critical}$, and α. The average α value from Table 2 (α=2.84) was used for all analyses in this study.
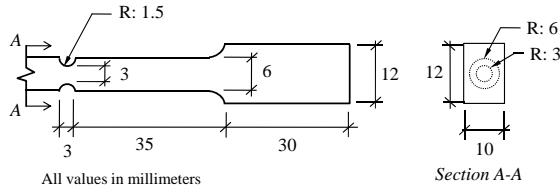
Figure 6. Nominal CNT specimen dimensions

Table 2: α Calibration Parameters and Results

| Specimen	D_{NR} [mm]	$D_{NR,f}$ [mm]	R_N [mm]	T'	$\varepsilon'_{p,critical}$	α
CNT 1	3.01	2.22	1.3	1.07	0.593	2.93
CNT 2	3	2.2	1.3	1.06	0.605	2.99
CNT 3	3	2.28	1.31	1.05	0.53	2.56
CNT 4	2.95	2.19	1.31	1.06	0.587	2.89

[*]Coefficient of variation   Mean α (COV[*]): 2.84 (0.07)

5. ANALYSIS RESULTS

5.1. Multi-Axial Membrane Demands

Combined circumferential and radial stresses have the potential to increase plastic strains in the base-plate when circumferential stresses are compressive (Prinz and Nussbaumer, 2012b). Figure 7 shows the distribution of circumferential stress versus base uplift for the Rumlang and Mellingen tanks. All circumferential stress values were taken from the base-plate centerline near the shell-to-base connection during the first uplift cycle (see diagram in Figure 7). For the slender Rumlang tank, the connection region experiences circumferential compressive stresses equal to 9% σ_y at the peak of the first uplift cycle. The broad Mellingen tank experiences little circumferential stress, with the peak value near 0.2% σ_y in circumferential tension. The large difference in circumferential base-plate stress can be attributed to the difference in tank geometry (the Mellingen tank radius is 7m larger than the Rumlang radius). Geometric effects due to uplift diminish as the base-plate radius of curvature increases.
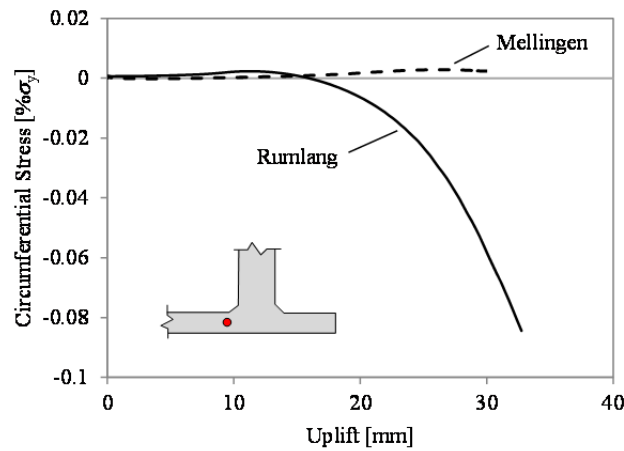
Figure 7. Circumferential stress versus uplift height for first uplift cycle.

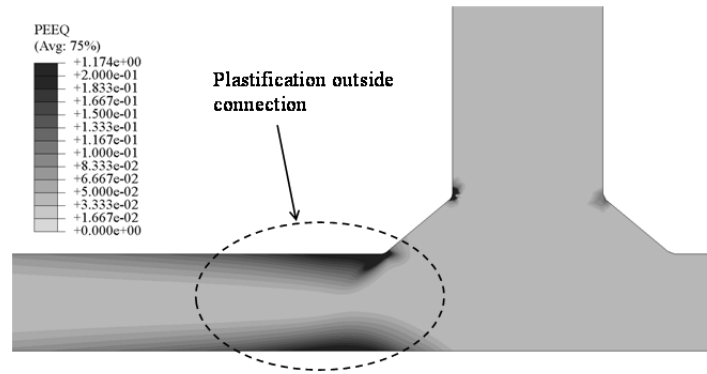## 5.2. Damage Accumulation and Connection Fatigue Assessment

Figure 8 shows the accumulation of plastic strain outside the weld geometry region in the Rumlang model. Both the top and bottom face of the tank base-plate plastify as tensile and compressive strains develop during bending. The highest concentration of plastic strain occurred on the base-plate upper face at the edge of the weld toe. This strain concentration is due to the change in section stiffness associated with the geometry reduction. During unloading, plastic strains at the base-plate lower face increased as the residual plate deformations were removed by contact from the simulated foundation. Similar patterns of accumulated plastic strain were observed in the Mellingen model.

Stress and strain data taken from the location of highest plastic strain (the element located at the weld-toe edge) were incorporated into the SMCS criterion to assess fatigue damage. Figure 9 shows the accumulation of the SMCS damage index for the Rumlang and Mellingen connections during the

different uplift histories. From Figure 9, the damage index for both tank connections remains below the critical value of 1, indicating that fracture initiation will not occur under the applied uplift demands. The damage index for the Rumlang tank following the uplift history is 0.953. The damage index for the Mellingen tank following the uplift history is 0.069. Assuming a linear accumulation of damage, the slender Rumlang tank could withstand only one earthquake prior to fracture initiation at the base-plate surface, while the broad Mellingen tank could be expected to withstand nearly 15 design-level earthquakes prior to initiation of fatigue fractures. It is important to note that experimental testing indicates significant connection capacity beyond the initiation of surface cracks (Cortes et al., 2011; Prinz and Nussbaumer, 2012a).

Rotation demands applied to the tank connections exceed current code limits. Calculation of the base-plate rotation depends on both uplift height (which is applied to the connection) and uplift length, which is determined from the ABAQUS model deformed shape. Equation 5.1 presents the relationship between uplift height, h, uplift length, L, tank radius, R, and the connection rotation $,\theta$ (Eurocode 8, 1998). Figure 10 shows the resulting connection rotation and uplift length for both the Rumland and Mellingen tanks during the peak uplift cycle. The peak connection rotation for the Rumlang and Mellingen tanks are 0.385rad and 0.297rad respectively. Current EC8 and NZSEE standards limit connection rotation to less than 0.2rad.
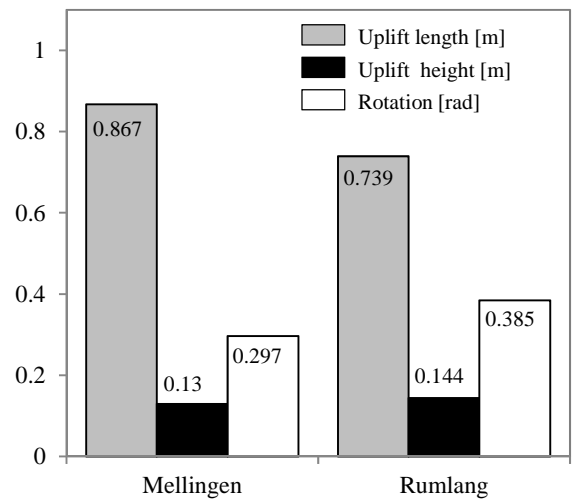
$$\theta = \frac{2u}{L} - \frac{u}{2R} \tag{5.1}$$

Figure 8. Plastic strain accumulation in Rumlang tank connection following uplift history.
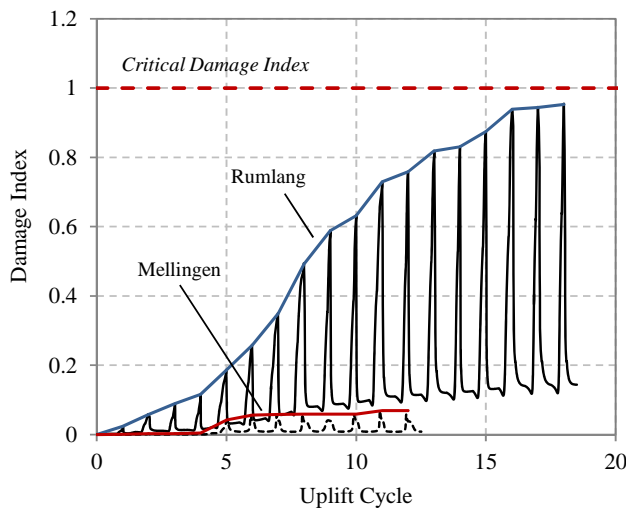
Figure 9. Damage index during uplift for Rumlang and Mellingen tank connections.

Figure 10. Uplift length and connection rotation corresponding to peak uplift height.

6. SUMMARY AND CONCLUSIONS

In this paper, two tank shell-to-base connection models are subjected to realistic variable range uplift histories generated from design-level earthquake ground motions. The two shell-to-base connections simulate both slender and broad tank geometries and are created based on existing tank connections from within Switzerland. A low-cycle fatigue damage index is calibrated for the tank base-plate material and the initiation of fatigue fracture is assessed following the loading histories. The damage index for both connection models remained below the critical damage index indicating that the fatigue capacity of the connection is greater than the demand from the design level earthquake. According to the fatigue model, the broad tank connection could withstand near 15 design level earthquakes prior to fracture initiation. Both connections sustained rotations greater than current code limits. With peak rotations between 0.29 and 0.38rad for the broad and slender tank connections, and with the fatigue damage index below the critical value for fracture initiation for the entire uplift history, the current code limit of 0.2rad appears overly conservative.

REFERENCES

ASTM (2002). Standard test methods for tension testing of metallic materials. E8,. West Conshohicken, Pa.

Cortes, G., Nussbaumer, A., Berger, C., and Lattion, E. (2011). "Experimental determination of the rotational capacity of wall-to-base connections in storage tanks." *J. Constructional Steel Research,*, 67(2011): 1174-1184.

Eurocode_8 (1998). "Part 1: General rules, seismic actions and rules for buildings." *ENV 1998-1*: European Committee for Standardization, Brussels, Belgium.

Eurocode_8 (1998). Part 4: Silos, Tanks, and Pipelines. ENV 1998-4,. European Committee for Standardization, Brussels, Belgium.

Fujikazu, S., Akira, I., Hajime, H., and Yukio, M. (1988). Experimental study on uplifting behavior of flat-based liquid storage tanks without anchors. Proc. 9th World Conference on Earthquake Engineering. Tokyo-Kyoto, Japan**:** 649-654.

Hancock, J. W., and Mackenzie, A.C. (1976). "On the mechanics of ductile failure in high-strength steel subjected to mulit-axial stress-states." *J. Mech. Phys. Solids*, 24(3): 147-160.

Kanvinde, A. M., and Deierlein, G.G. (2004). Micromechanical simulation of earthquake induced fractures in steel structures. Blume Center TR145. Stanford, CA, Stanford Univ.

Kanvinde, A. M., and Deierlein, G.G. (2006). "Void growth model and stress modified critical strain model to predict ductile fracture in structural steels." *J. Struct. Eng.*, 132(12): 1907-1918.

Koller, M.G., and Malhotra, P.K. (2004). "Seismic evaluation of unanchored cylindrical tanks." *13th World Conference on Earthquake Engineering*, Vancouver, B.C., Canada.

Koller, M.G. (2003). "Erdbebensicherheit bestehender unverankerter stehtanks in bezug auf storfallrelevante schaden." *Report No. TB 245-02/MK*. Resonance Ingenieurs-Conseils.

McKenna, F. (1997). "Object oriented finite element programming frameworks for analysis, algorithms and parallel computing." *Ph.D. Dissertation,* University of California, Berkeley, CA.

Myers, A. T., Kanvinde, A.M., and Deierlein, G.G. (2010). "Calibration of the SMCS criterion for ductile fracture in steels: specimen size dependence and parameter assessment." *J. Eng. Mech.*, 136(11): 1401-1410.

NZSEE (2009). Seismic Design of Storage Tanks. New Zealand National Society for Earthquake Engineering Wellington, New Zealand.

Peek, R. (1988). "Analysis of unanchored liquid storage tanks under lateral loads." *Earthquake Eng. and Struct. Dyn.*, 16: 1087-1100.

Peek, R., and Jennings, P.C. (1988). "Simplified analysis of unanchored tanks." *Earthquake Eng. and Struct. Dyn.*, 16: 1073-1085.

Prinz, G. S., and Nussbaumer, A. (2012a). "Seismic performance of unanchored liquid storage tank shell-to-base connections -- Phase 2." *Rapport de mandat No. 174640*: Ecole Polytechnique Federale de Lausanne (EPFL), Lausanne, Switzerland.

Prinz, G. S., and Nussbaumer, A. (2012b). "Fatigue analysis of liquid storage tank shell-to-base connections under multi-axial loading." *Eng. Structures*, 40: 75-82.

Sabetta, F., and Pugliese, A. (1996). "Estimation of response spectra and simulation of nonstationary earthquake ground motions." *Bulletin of the Seismological Society of America*, 86(2): 337-352.